Air Gap Measurement During Steel-Ingot Casting and Its Effect on Interfacial Heat Transfer

WANMING LI, LEIJI LI, YIFENG GENG, XIMIN ZANG, YU'AN JING, DEJUN LI, and BRIAN G. THOMAS

Air gap formation during solidification greatly affects interfacial heat transfer and both must be understood quantitatively for accurate numerical simulation of casting processes, which are needed for fundamental understanding to enable quality improvements. Displacement and temperature in a 23 kg steel ingot and mold were measured simultaneously during solidification using a new experimental system. Interfacial heat transfer coefficients were extracted from the measurement results using an inverse heat conduction model. The evolution of temperature, air gap thickness, and interfacial heat transfer coefficients (IHTC) were quantified during this ingot casting process. The air gap forms earlier and grows larger on the narrow side than on the width side of the ingot. Interfacial heat transfer can be divided into four stages. In the first stage, there is good contact between the steel shell and the mold, so there is no air gap, and IHTC is high: 2700 to 3000 W m^{-2} °C^{-1}. In the second stage, an air gap starts to form, so heat transfer decreases sharply. In the third stage, as the air gap thickness continues to grow, its effect weakens. In the fourth stage, even as the air gap continues to grow, IHTC remains almost constant at about 600 W m^{-2} °C^{-1}. The IHTC can be predicted reasonably well with a simple equation based on conduction across the measured gap thickness, radiation, and contact resistance based on the measured roughness of the cast surface. Conduction is more important than radiation across the gap, accounting for about seventy percent of the effective IHTC at later times when the gap is large.

https://doi.org/10.1007/s11663-021-02152-3

I. INTRODUCTION

THE interfacial heat transfer coefficient (IHTC) between the casting and mold is important to ingot solidification and product quality. During the solidification process, the ingot solidifies and shrinks in the mold, forming an air gap between the casting and the mold. The size of this air gap controls the heat transfer and temperature distribution.[1–4] This in turn controls the cooling rate, thermal stresses, grain structure,[5] and ultimately the ingot quality.[6] Ingot quality defects[7–9] such as center porosity, segregation, and coarse crystals often arise during the solidification process and are affected by taper of the mold walls.[10,11] However, due to the lack of quantitative understanding of the formation of the air gap, there is no theoretical basis to optimize the mold taper.

The IHTC is an important parameter, needed for accurate numerical simulation of temperature evolution and solidification during casting processes. Lacking knowledge of the air gap formation details, previous heat transfer models of ingot casting have mainly used empirical relations for the interfacial heat transfer.[12–16] Sarjant[4] developed early finite-difference heat transfer models of ingot casting and predicted that air gap formation greatly hindered interfacial heat transfer. A previous finite-element model investigation of heat transfer in steel ingots[17] applied a relation for IHTC that included radiation and conduction operating together, where the gap conductivity dropped linearly from 1700 W m^{-2} °C^{-1} at the time the molten metal contacts the mold to zero at time t_{gap}, which increased

WANMING LI is with the University of Science and Technology Liaoning, Anshan, 114051, People's Republic of China, and also with the Department of Mechanical Engineering, Colorado School of Mines, Golden, CO, 80401. LEIJI LI, YIFENG GENG, XIMIN ZANG, and YU'AN JING are with the University of Science and Technology Liaoning. DEJUN LI is with State Key Laboratory of Marine Engineering, Ansteel Group, Anshan, 114051, People's Republic of China. BRIAN G. THOMAS is with the Department of Mechanical Engineering, Colorado School of Mines. Contact e-mail: bgthomas@mines.edu
Manuscript submitted December 14, 2020; accepted March 13, 2021.

Published online: 07 May 2021

with distance from the ingot corner, d, according to previous measurements of gap formation time by Oeters *et al.*[18]: $t_{gap}(s) = 50 + 10{,}800\,[d(m)]^{1.6}$.

Owing to its important effect on the IHTC, several previous studies[18–20] have measured temperature and air gap formation histories during ingot casting. Many researchers believe that gap formation is due to thermal contraction of the solidifying shell after it is strong enough to overcome the metallostatic pressure.[19,21–23] Kron *et al.*[20] concluded that the formation and condensation of lattice defects are important factors to consider in air gap formation. Engler *et al.*[24] concluded that the volume expansion of eutectic gray cast iron due to the precipitation of graphite in solidification reduces the air gap size.

Several models have simulated thermal-mechanical behavior during ingot casting, including formation of the air gap, and its coupled effect on interfacial heat transfer, using analytical solutions,[22] finite-element analysis,[14,18,19] and other computational methods.[15,16] Several early researchers[25–27] assumed that the mold wall was rigid, and calculated ingot solidification and shrinkage to estimate the air gap. Fredriksson and coworkers[20,28–31] modeled the effects of crystal lattice defects and vacancy condensation on shrinkage during solidification and its effect on air gap formation. Clearly, air gap formation greatly affects interfacial heat transfer, but the phenomena are complex. To quantify the IHTC due to air gap formation, careful laboratory measurements should be combined together with computational models.

Dong *et al.*[32] studied the solidification of a single-crystal turbine blade and found that IHTC decreased rapidly when the air gap started to form. Several researchers have used trial and error to fit the transient IHTC from such models to the form: $h_k = C_k(t)^{-n}$.[32–34] However, inverse methods enable more accurate tracking of the measured temperatures, to find a more accurate IHTC history. Milano *et al.*[35] modified the least-squares technique to include a *Maximum A Posteriori* (MAP) algorithm. Rappaz *et al.*[36] implemented a MAP algorithm into a direct finite-element model of transient heat flow during aluminum-copper alloy ingot solidification. Drezet *et al.*[37] adapted an inverse method based on a MAP algorithm to the steady-state temperature field to get the heat flux on the ingot surface. However, none of these inverse model studies provide insight into the air gap.

In this paper, temperature and displacement in a steel-ingot casting and mold are measured during the entire solidification process using a novel in-house experimental system. The evolution of the air gap thickness and temperature with time is measured, and final surface roughness is measured. Based on the measurements, the interfacial heat transfer coefficient history is obtained by inverse model simulations of transient heat transfer in the solidifying ingot and mold, using ProCAST software. The effect of air gap thickness on interfacial heat transfer coefficient is then quantified with a simple model.

II. EXPERIMENTAL SETUP

An in-house experimental device was constructed to simultaneously measure the temperature, displacement, and air gap evolution at particular locations on the surfaces of the ingot and mold wall during solidification, as shown in Figure 1. The mold sides are welded together from steel plates with a thickness of 10 mm. The mold cavity is 180 mm in width, 90 mm in thickness, and 240 mm in height. Both the mold sides and molten metal ingot are Q235 steel, with composition listed in Table I. MgO firebrick was used to insulate the bottom of the casting. The steel is melted in a non-vacuum induction furnace at 1600 °C and poured into the top of the mold. Ceramic asbestos insulation boards are

Table I. Composition of Q235 Steel Used in the Experiment

Constituent Elements	C	Si	Mn	P	S	Fe
Content (wt pct)	0.15	0.13	0.43	0.035	0.025	bal.

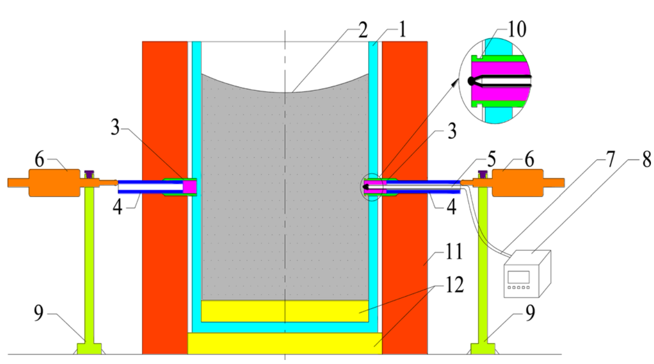

1.Mold; 2. Ingot; 3. Stainless Steel tube; 4. Quartz tube; 5. Thermocouple; 6. Dial indicator; 7. Copper compensation wire; 8. Temperature indicator; 9. Bracket; 10. Connecting rod; 11. Ceramic asbestos; 12. MgO firebrick

Fig. 1—In-house system to measure temperature and displacement in casting and mold during steel-ingot casting.

mounted near to the mold exterior to protect the measuring instruments from excessive heat, while leaving a 5 mm gap to enable heat to escape vertically.

In order to simultaneously measure the temperature and displacement of the ingot at 5 seconds time intervals during the solidification process, a 16.5-mm-diameter hole was made completely through the mold plate at each measurement location. A connecting rod device consisting of a B-type thermocouple contained in a 12-mm-diameter quartz tube inside a 16-mm-diameter steel tube is inserted through the hole, as shown in Figure 2, to protrude into the mold cavity. Grooves near the end of the steel tube cause the initial shell of the ingot to solidify rigidly around the connecting rod. The other end of the connecting rod connects to a dial indicator, which accurately shows the shrinkage displacement of the ingot. The measurement devices were installed in two planes in the narrow and wide mold plates located (1) 110 mm above and (2) 90 mm above the bottom surface of the mold cavity. Temperature was measured at all 6 locations (A, B, C, D, E and F) in the ingot, shown in Table II and Figure 3, while temperature and displacement were both measured together only at point B/B_1 (wide side) and point E/E_1 (narrow side). The subscript "1" indicates a displacement measurement point. Note that points B and B_1 have the same location, as do E and E_1.

Similarly, to measure temperature and displacement in the mold wall, a 4-mm-deep hole with a diameter of 16.5 mm was made into the exterior of the mold plate. By pushing the 16-mm-diameter connecting rod device in to contact the bottom of the hole, displacement of the ingot-mold surface was transferred to the dial indicator and recorded. These connecting rods contained K-type thermocouples within the 4-mm-diameter protective sleeve to measure temperature variation in the mold. As shown in Table II and Figure 3, temperature was measured at point H (wide side) and point J (narrow side), and displacement was measured at two nearby locations, point G_1 (wide side) and point I_1 (narrow side).

In order to include the effect of roughness on the interfacial heat transfer coefficient, the roughness of the surface of the steel ingot was measured using a dial gage with a sharp point (0.18-micron-tip diameter), as shown in Figure 4(a). For the test, a grid of 10 mm ×10 mm squares was drawn on the each ingot surface, as shown in Figure 4(b), and the depth at each grid intersection point was recorded. A total of 63 data points were measured on each ingot face. An example of the measured roughness data, y_i is given in Table III. The average roughness, R_q, was found using Eq. [1] to be 0.249 mm on the wide side and 0.252 mm on the narrow side.

$$R_q = \sqrt{\frac{1}{n}\sum_{i=1}^{n}(y_i - \bar{y})^2}, \qquad [1]$$

where n is the number of measurements and $\bar{y}$ is the mean of the dataset, for each side.

III. MATHEMATICAL MODEL OF INGOT SOLIDIFICATION AND HEAT TRANSFER

A three-dimensional finite-element model of transient heat conduction was applied in this work to simulate temperature histories of the solidifying ingot and mold, which incorporates an inverse model to ensure that the

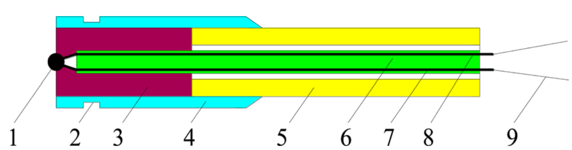

1. Measuring bead; 2. Groove; 3. Magnesite bonded with sodium silicate; 4. Stainless steel tube; 5. Quartz tube;

6. Corundum tube; 7. Platinum-30% Rhodium wire; 8. Platinum-6% Rhodium wire; 9. Copper wire

Fig. 2—Close-up of Connecting Rod for Simultaneous Measurement of Temperature and Displacement

Fig. 2—Close-up of connecting rod for simultaneous measurement of temperature and displacement.

Table II. Location of Measurement Points in the Casting and Mold

Casting and Mold Surface	Ingot						Mold	
	Wide Side			Narrow Side			Wide Side	Narrow Side
Temperature Measurement Point	A	B	C	D	E	F	H	J
Displacement Measurement Point		B_1			E_1		G_1	I_1
Distance from the Interface (mm)	25	5	15	25	5	15	5	5

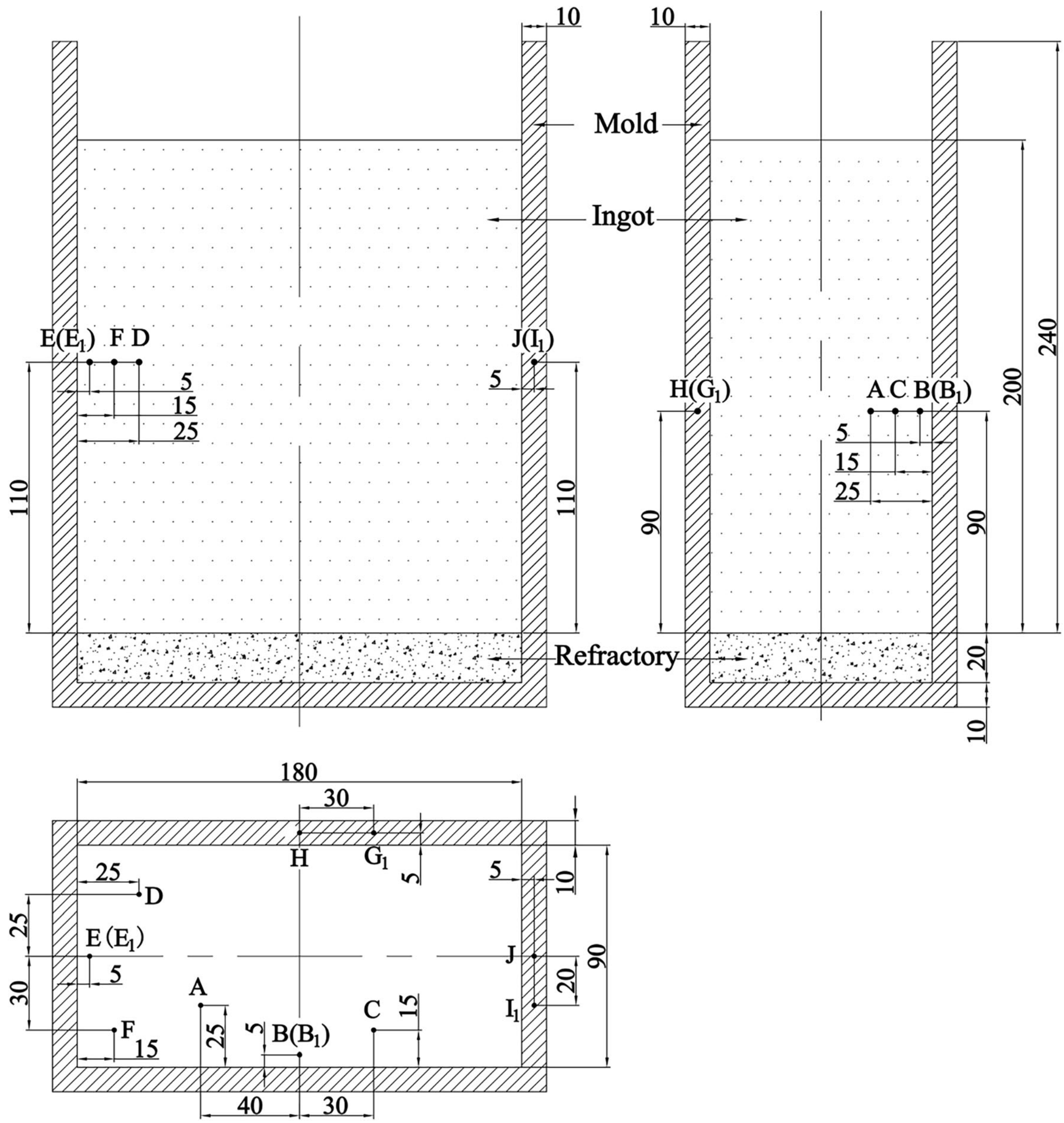

Fig. 3—Ingot geometry showing location of temperature and displacement measurement points (unit: mm).

Fig. 4—Roughness measurements (*a*) measuring device, and (*b*) grid of measured points on ingot surface.

predicted temperatures exactly match the measured temperatures at specified locations in the ingot and mold.

A. *Governing Equations*

Based on the energy conservation law, the three-dimensional transient heat conduction equation can be solved to obtain the temperature distribution in the ingot and mold:

$$\rho C_{\mathrm{p,eq}} \frac{\partial T}{\partial t} = \nabla \cdot (k \nabla T), \qquad [2]$$

where ρ is the density, kg m^{-3}; k is the thermal conductivity, W m^{-1} °C^{-1}; and $C_{\mathrm{p,eq}}$ is the effective heat capacity that includes the latent heat of solidification when inside the mush zone:

$$C_{\mathrm{p,eq}} = C_{\mathrm{p}} - L_{\mathrm{m}} \frac{\partial f_{\mathrm{s}}}{\partial T}, \qquad [3]$$

where C_{p} is the heat capacity at constant pressure, J kg^{-1} °C^{-1}; L_{m} is the latent heat of solidification per unit mass of metal, J kg^{-1}; f_{s} is solid fraction; and t is time, s. The internal boundary condition for these equations applied at the ingot/mold interface is

$$-k\nabla T\big|_{\text{ingot surface}} = h(T_{\mathrm{I}} - T_{\mathrm{M}}) = k\nabla T|_{\text{mold surface}} \qquad [4]$$

where h is the macroscopic average ingot/mold interfacial heat transfer coefficient (IHTC) across the interfacial gap of most interest in this work, W m^{-2} °C^{-1}; T_{I} and T_{M} are the ingot surface temperature and the inner wall temperature of the mold, respectively.

The mold exterior is subject to a convection boundary condition:

$$-k\nabla T|_{\text{Mold exterior}} = h_{\mathrm{a}}(T_{\mathrm{Ma}} - T_{\mathrm{a}}), \qquad [5]$$

where h_{a} is the heat transfer coefficient for turbulent air flow over vertical surfaces, 10 W m^{-2} °C^{-1}, chosen from previous successful work.[38] The ambient temperature, T_{a}, is set to 5 °C air for winter, and T_{Ma} is the unknown surface temperature of the mold exterior. Similar boundary conditions are applied at the top surface of the molten steel, and at the bottom surface of the insulating firebrick refractory, but these boundary surfaces are too far away to have much influence on the region of interest midway up the ingot where the sensors are located.

These equations are discretized in space using the finite-element method and solved for the nodal temperatures, T_{n}, incrementally in time, t_{r} using a finite-difference method, with a small time step size Δt_{r}.

B. *Inverse Model*

The temperature at a given node T_n^m near the interface of the ingot or mold where a temperature measurement was made can be approximated using a first-order Taylor Series expansion with respect to the closest local interfacial heat transfer coefficient as follows:

$$T_n(h_k) = T_n(h_{k,0}) + \frac{\partial T_n(h_k)}{\partial h_k}(h_k - h_{k,0}), \qquad [6]$$

where $h_{k,0}$ is the initial estimate of IHTC, h_k and n is the node number. Using nonlinear inverse modeling to find the best values for the unknown IHTCs, its basic idea is to estimate IHTC at time t using measured temperature values (found by linear interpolation between the recorded temperature measurements). To better estimate the derivatives, the simulation proceeds for r extra future time steps after t, and IHTC is kept constant during this time interval from t to $t+(r-1)\times\triangle t$.

Starting from $h_{k,0}$, a least-squares fitting algorithm is adopted to repeatedly adjust the unknown h_k values until the deviations, S, between the calculated and ''measured'' temperature values are small, according to minimizing the objective function in Eq. [7],

$$S(h_{k,t}) = \sum_{n=1}^{N}\sum_{j=0}^{r-1}\left[T^m_{n,t+j\times\Delta t} - T^c_{n,t+j\times\Delta t}(h_{k,0,t})\right]^2 + \beta(h_{k,t} - h_{k,0,t})^2, \qquad [7]$$

where $T^m_{n,t+j\times\Delta t}$ is the measured temperature value at node n at time $t + j \times \triangle t$, and $T^c_{n,t+j\times\Delta t}(h_{k,0,t})$ are temperatures calculated using $h_{k,t}$; N is the total number of measurement nodes, and r is the number of extra future time steps considered during this inverse modeling loop. The first term on the right in Eq. [7] is the least-squares expression for the error and the second term is for stability. The stability factor β is set to 10^{-10}.

In the optimization process, the objective function $S(h_k)$ is minimized with respect to the heat transfer coefficients, $\partial S(h_k)/\partial h_k = 0$ and Eq. [7] can be rewritten as follows:

Table III. Roughness Measurements, y_i, on 70 mm × 90 mm Grid on Ingot Wide Side (mm)

0.46	0.35	0.31	0.28	0.33	0.27	0.4	0.55	0.58
0.45	0.32	0.08	− 0.15	− 0.12	− 0.02	0.05	0.22	0.38
0.29	0.19	0.03	− 0.12	− 0.16	− 0.14	− 0.08	− 0.04	0.15
0.51	0.39	0.23	0.15	0	0.01	− 0.02	0.1	0.13
0.59	0.57	0.38	0.3	0.03	0.2	0.11	0.13	0.2
0.78	0.65	0.49	0.44	0.43	0.32	0.3	0.28	0.16
0.88	0.83	0.73	0.32	0.56	0.57	0.46	0.2	0.24

$$\sum_{n=1}^{N}\sum_{j=0}^{r-1}\left[T^{m}_{n,t+j\times\Delta t}-T^{c}_{n,t+j\times\Delta t}\right]^{2}X_{k,n,t+j\times\Delta t} = \beta(h_{k,t}-h_{k,0,t})^{2}, \quad [8]$$

where

$$X_{k,n,t+j\times\Delta t}=\frac{T^{c}_{n,t+j\times\Delta t}[h_{k,t}+\varepsilon h_{k,t}]-T^{c}_{n,t+j\times\Delta t}(h_{k,t})}{\varepsilon h_{k,t}}, \quad [9]$$

where $X_{k,n,t+j\times\Delta t}$ are sensitivity coefficients, Δt is the small time step for the forward heat transfer calculation, and constant ε is small (0.001), to obtain accurate $X_{k,n,t+j\times\Delta t}$ values. Calculated temperatures $T^{c}_{n,k+j}[h_k+\varepsilon h_k]$ and $T^{c}_{n,k+j}(h_k)$ are found by solving the temperature field equation twice each time step using IHTCs $h_{k,t}+\varepsilon h_{k,t}$ and $h_{k,t}$.

Substituting Eqs. [8] and (9) into Eq. [7] and rearranging gives

$$h_{k,t}=h_{k,0,t}+\frac{\sum_{n=1}^{N}\sum_{j=0}^{r-1}\left[T^{m}_{n,t+j\times\Delta t}-T^{c}_{n,t+j\times\Delta t}(h_{k,0,t})\right]X_{k,n,t+j\times\Delta t}}{\sum_{n=1}^{N}\sum_{j=0}^{r-1}(X_{k,n,t+j\times\Delta t})^{2}+\beta}. \quad [10]$$

This inverse calculation procedure is summarized in the flow chart in Figure 5, where Eqs. [2], (9), and (10) are solved by ProCAST. First, temperature is calculated *via* a standard forward calculation for a short time interval, by solving Eq. [2] with boundary conditions found using the initial estimate for IHTC of $h_{k,0}$. These calculated temperatures are used to find sensitivity coefficients $X_{k,n,t+j\times\Delta t}$ according to Eq. [9]. Next, the average ingot/mold IHTC $h_{k,t}$ is obtained from Eq. [10] based on $h_{k,0}$ and$X_{k,n,t+j\times\Delta t}$. Finally, the estimate is updated, $h_{k,0,t}=h_{k,t}$and the procedure is repeated until meeting the convergence criterion:

$$\left|\frac{h_{k,t}-h_{k,0}}{h_{k,t}}\right|=|\Delta h/h|<0.001=C. \quad [11]$$

The calculated temperatures, T_t and IHTC, $h_{k,t}$ are output for time t, and the calculation proceeds to the next small time step. The initial estimate is changed according to Table V at large time intervals, which is tracked using $t_{\max}$.

C. *Model Implementation*

Figure 5 shows the flow chart for the thermal solidification model in this work, including the inverse model calculation of the interfacial heat transfer coefficients. The entire 3-D geometric model and mesh were created according to the dimensions in Figure 3, but only half of the domain is shown in Figure 6 in order to better visualize the grid for each domain. The mesh consists of 397,574 four-node tetrahedral finite elements. Temperature-dependent thermal properties of the ingot and mold are given in Table IV. The liquidus temperature of Q235 steel is taken as 1522 °C and solidus temperature as 1483 °C, using the ProCAST material database.

To start the simulation, the initial ingot temperature is set to the pour temperature, 1600 °C, while the initial mold temperature is set to 10 °C. Then, a forward calculation is run using ProCAST, based on initial values of the interfacial heat transfer coefficients h_k^0 to define the unknown internal boundary conditions, as given in Table V. Next, the measured temperature histories of the ingot and mold surface temperatures obtained from the experiment are input as fixed temperatures into the boundary condition equation, Eq. [5] according to their grid node number, while h_k is left unknown. Then, the inverse model is run, selecting the option representing the ingot-mold interface boundary condition in ProCAST, and iteration proceeds until convergence is reached. A maximum number of iterations for k, ITERMAX, of 15 was sufficient. Parameters for this calculation are given in Table VI. Finally, the calculated interface heat transfer coefficients are output, in addition to the corresponding temperature histories in both the ingot and mold.

IV. RESULTS AND ANALYSIS

Temperature and displacement histories in the ingot and mold are obtained during the solidification process from in-house experimental measurements. Temperature evolution is simulated using the transient finite-element model, based on IHTC obtained at different times using inverse model calculations. The IHTC values are verified by a forward calculation. The relationship between IHTC and temperature, displacement, and air gap thickness is systematically analyzed. Finally, simple model of the relationship between gap thickness and IHTC is obtained.

A. *Measured Temperature of Ingot and Mold*

The temperature histories measured at four locations each in the ingot and mold are shown in Figure 7, starting from time zero when the molten steel was poured into the mold. Figure 7(a) shows temperature of the measurement points on the narrow surface of the ingot, and Figure 7(b) shows those on the wide surface. After pouring molten steel into the mold, temperature measured in both the ingot and mold is seen to rise rapidly and then decrease. The maximum temperature reached at each point on the narrow and wide surfaces, and their corresponding time is shown in Tables VII and VIII, respectively.

Temperature in the ingot increases rapidly, according to the thermocouple response time, which takes about 76 seconds. The deeper the thermocouple bead is inserted into the ingot, the higher is the maximum temperature, and the longer the high temperature is maintained. This is because temperature near the ingot surface has already started to cool before the thermocouple has heated up. The maximum temperature of

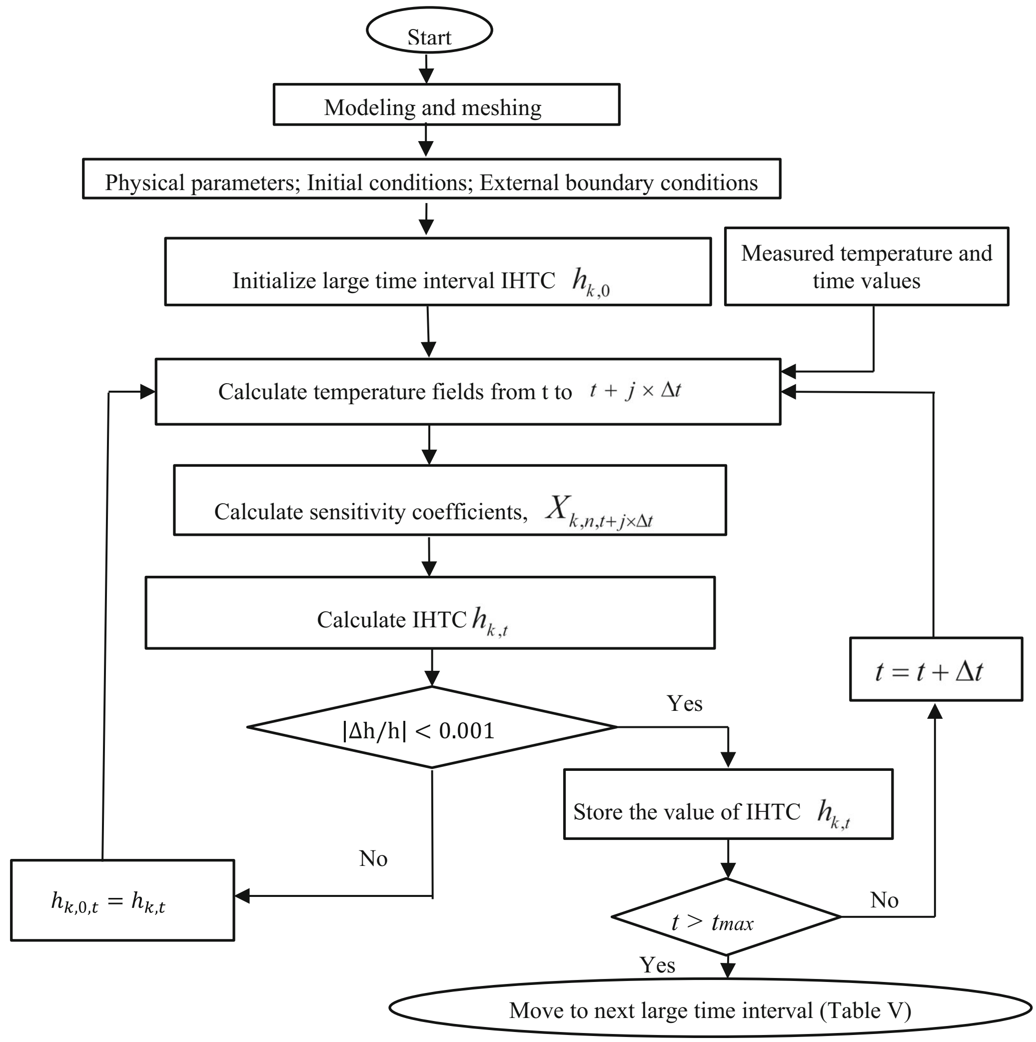

Fig. 5—Flow chart of model calculation of temperature and interfacial heat transfer coefficient.

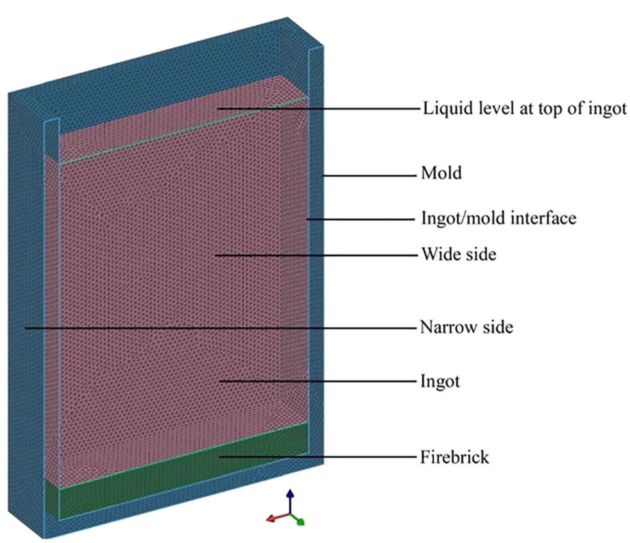

Fig. 6—Cutaway view of simulation domain and mesh of ingot and mold.

points B and E is lower than that of other points in the ingot. This may be due to the closeness of the mold wall here, and the solidified shell is quickly formed. Temperature in the wide side of the ingot is significantly lower than that on the narrow surface, because the heat transfer distance is shorter and the heat transfer is faster.

Temperature in the mold increases more slowly, as the mold heats up, according its thermal properties and dimensions. Mold temperature, measured at points H and J, reaches a maximum after about 437 and 365 seconds, respectively, and begins to decrease, which means that the heat entering the mold at this time starts to be less than heat lost to the surroundings.

B. *Measured Displacement of Ingot and Mold*

Displacement histories measured at two points each in the ingot and mold are shown in Figures 8 and 9, respectively, together with the corresponding temperature measurements for comparison. Positive displacement represents expansion away from the ingot interior. Temperature and displacement are observed to evolve in a similar fashion, except near the very beginning. This indicates that the temperature is the main factor affecting the change of displacement.

After pouring starts, the mold expands as it heats up, causing positive displacement. The ingot displacement is also positive, as the molten steel follows the expanding mold. During this stage, the molten steel level decreases accordingly. Expansion displacement of the ingot reaches a maximum after about 110 seconds, of 0.99 mm and 1.55 mm on the wide side and narrow side, respectively. After that, the solidified shell at the surface of the ingot is strong enough to support the internal ferrostatic pressure, and it loses contact with the mold. As the shell strengthens and cools, it starts to shrink, as indicated by the negative displacement observed at the ingot surface.

It is worth noting that during the early stage of solidification, the strength of the bond between the initially solidified shell and the connecting rod may be weak, so the connecting rod can still expand with the mold. After more crystals have solidified a strong skeleton around the connecting rod, the displacement shows shrinkage of the solid shell, which proceeds linearly with time.

Displacement measured in the mold in Figure 9 shows that the maximum mold expansion occurs about 100 seconds before the temperature peak. The shrinkage rate decreases suddenly to almost zero when the temperature drops to about 800 °C. This may be due to the eutectoid phase transition from austenite at this temperature and the accompanying volumetric expansion.

After 2400 seconds, as seen in Figures 8 and 9, the mold displacement becomes almost constant, but the ingot expands slightly. This may be due to the expansion that accompanies the austenite to ferrite phase transformation near the surface region of the steel ingot during this time. The net result is a slight decrease in the gap thickness with time, which is discussed in more detail in the next section.

C. *Analysis of Gap Measurements*

Temperature, displacement, and gap formation on the narrow side and wide side are shown in Figures 10 and 11, respectively. The gap thickness is calculated from the difference between the measured displacements of the surface of the ingot and the inner wall of the mold. During the early stage of molten steel pouring into the mold, the ingot surface contacts the inner wall of the mold due to the static pressure of the molten steel. For about 160 seconds, ingot and mold expand together, which is compensated by a decrease in liquid level. After that time, heat extraction by the mold causes a solidified shell to form on the surface of the ingot. As the solidified shell thickens, after about 100 seconds, it becomes strong enough to support the internal ferrostatic pressure of the molten steel and starts to shrink away from the mold to form a gap. This decreases heat flow into the mold, which halts the mold expansion, and after about 400 seconds, the mold starts to shrink as well. With continued cooling of the ingot and mold, the faster shrinkage of the shell causes the gap thickness to increase almost linearly from 160 to 2000 seconds. After about 2400 seconds, the gap thickness reaches a maximum and then slowly decreases.

To validate the *in situ* displacement measurements, after the ingot and mold completely cooled to room temperature, the system was carefully dissected and the gap thickness at the sensor height of 110 mm was measured, as shown in Figure 12. The measured thickness of the gap on the narrow side is 2.1 mm and the one on the wide side is 1.2 mm. This is close to the final measurements from the rods in Figures 10 and 11. This confirms that the air gap evolves during solidification, according to the measurements presented here.

Figure 13 shows the air gap change with time on the narrow side and wide side. Air gap thickness is observed to increase almost linearly with time from its formation time at about 100 to 2400 seconds. During the 100 seconds contact period, the air gap on the wide surface is slightly negative, which indicates the extent of combined errors in the ingot and mold displacement measurements. The cause may be expansion of the stainless steel tube in the displacement measurement device, leading to exaggeration of the measured ingot expansion, by ~0.2 mm.

To quantify growth of the air gap, a linear curve fit of the results in Figure 13 gives the following relationship between the gap thickness and time on the narrow side and wide side:

$$\delta_{NF} = 0.00152t + 0.03921, \ 100 \text{ s} < t < 2400 \text{ s}, \qquad [12]$$

$$\delta_{WF} = 0.00113t + 0.01574, \ 100 \text{ s} < t < 2400 \text{ s}, \qquad [13]$$

where δ_{NF} is the air gap thickness on the narrow side, mm; δ_{WF} is the air gap thickness on the wide side; mm; t is time, seconds.

D. *Inverse Model Validation*

The evolution of temperature and interfacial heat transfer coefficient, IHTC, with time is obtained from the finite-element simulation with the inverse model. To verify its accuracy, the IHTC history was re-imported into the PROCAST model. The temperature histories obtained from this standard, forward simulation are compared with the measured temperature histories at several locations in Figures 14(a) and (b). As can be seen from the figure, the simulated and measured values are in good agreement.

E. *Inverse Model Interfacial Heat Transfer Coefficients*

The predicted IHTC histories are plotted in Figures 15 and 16 together with the displacements of the ingot and mold, to illustrate the effect of changing air gap on IHTC. The gap and corresponding IHTC evolve in four stages, which are labeled according to time ranges by vertical dashed lines in Figures 15 and 16.

Table IV. Thermal Properties of Q235 Steel at Various Temperature Segments[39]

Temperature (°C)	20	250	500	750	1000	1500	1700	2500
Thermal Conductivity (W m^{-1} $°C^{-1}$)	50	47	40	27	30	37	140	142
Density × 10^3 (kg m^{-3})	7.8	7.7	7.61	7.55	7.49	7.35	7.3	7.09
Specific Heat Capacity (J kg^{-1} $°C^{-1}$)	460	480	530	675	670	660	780	820

Table V. Initial Interfacial Heat Transfer Coefficient with Time $h_{k,0}$

Time (s)	0	20	100	250	500	1000	1200	1480	1600	1950
Initial Interface Heat Transfer coefficient (W m^{-2} $°C^{-1}$)	2500	2500	2100	1750	1350	1000	900	750	650	600

Table VI. Inverse Model Parameters

Parameter	Parameter Meaning	Parameter Value
CONV	convergence tolerance, C	0.001
VARB	stability variation factor β	0.1
ITERMAX	max number of iterations per time step, max k	15
$\triangle t$	time step size, $\triangle t$	0.1 s
r	number of extra time steps during iteration for h	10

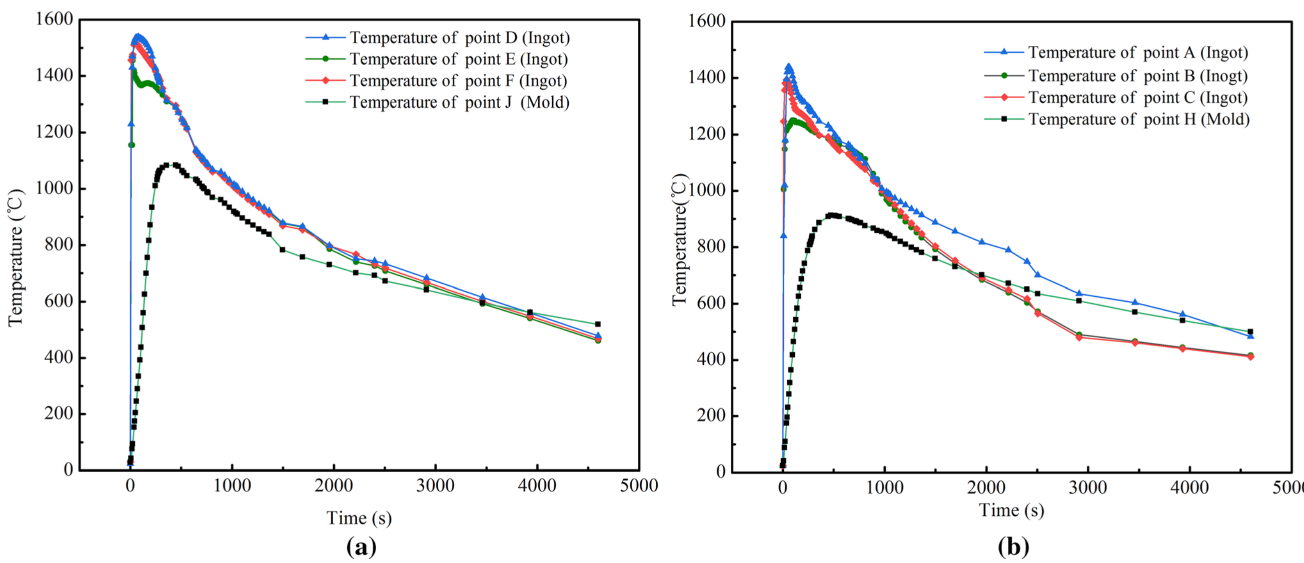

Fig. 7—Measured temperature histories in the ingot and mold (*a*) narrow side, and (*b*) wide side.

Table VII. Maximum Temperature Measured on Narrow Side

Measurement Point temperature	E	F	D	J (mold)
Maximum Temperature (°C)	1455	1516	1539	1084
Time (s)	23	51	81	446

In the first stage (a), the only resistance to heat flow is the surface roughness, so IHTC at this stage is the largest at ~3000 W m^{-2} °C^{-1}. The IHTC decreases slightly during this stage, owing to the decrease of surface temperature, and corresponding decrease in radiation. This stage lasts almost 100 seconds. In the second stage (b), the mold and ingot begin to separate and form an air gap. The formation of a true air gap causes the IHTC to decrease rapidly as the gap grows rapidly. This stage lasts about 200 seconds. The third stage (c) starts after complete solidification of the ingot (as seen in Figure 17), which occurs at 318 to 1600 seconds. This event has little effect on interfacial heat transfer. However, the IHTC decreases more slowly in this stage, as the gap grows more slowly. In the fourth stage (d), the gap stops growing and IHTC stays at about 600 W m^{-2} °C^{-1}.

Table VIII. Maximum Temperature Measured on Wide Side

Measurement Point	B	C	A	H (mold)
Maximum Temperature (°C)	1250	1394	1439	913
Time (s)	95	37	61	472

F. *Simple model of Interfacial Heat Transfer Coefficient*

Heat transfer across the interfacial air gap occurs by two parallel mechanisms: conduction, h_{cond} and radiation, h_{rad}:

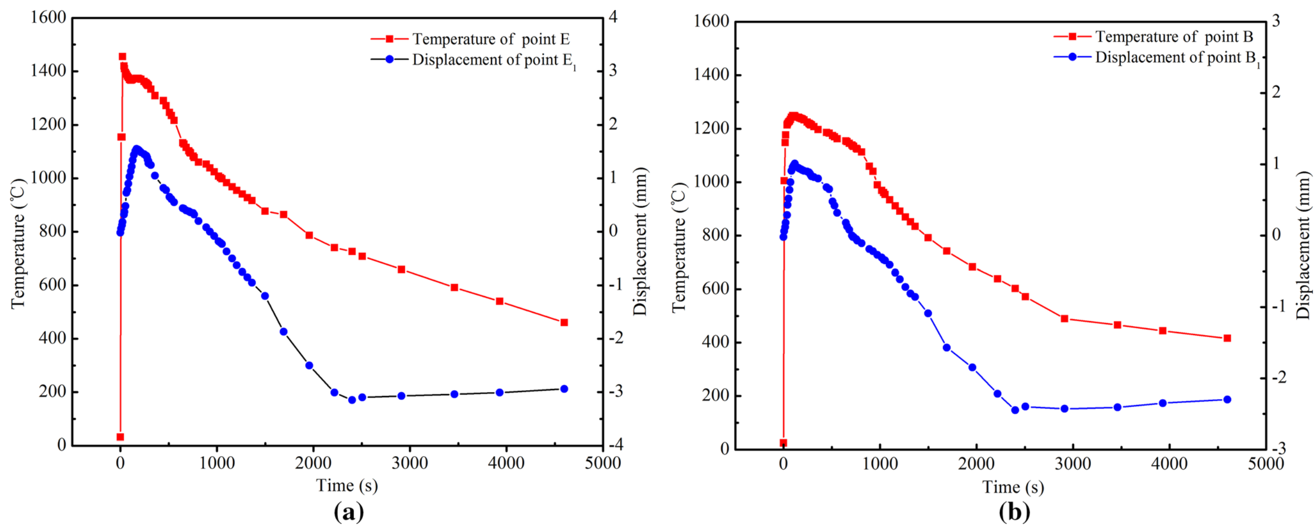

Fig. 8—Ingot temperature and displacement histories measured near casting surface (*a*) narrow side; (*b*) wide side.

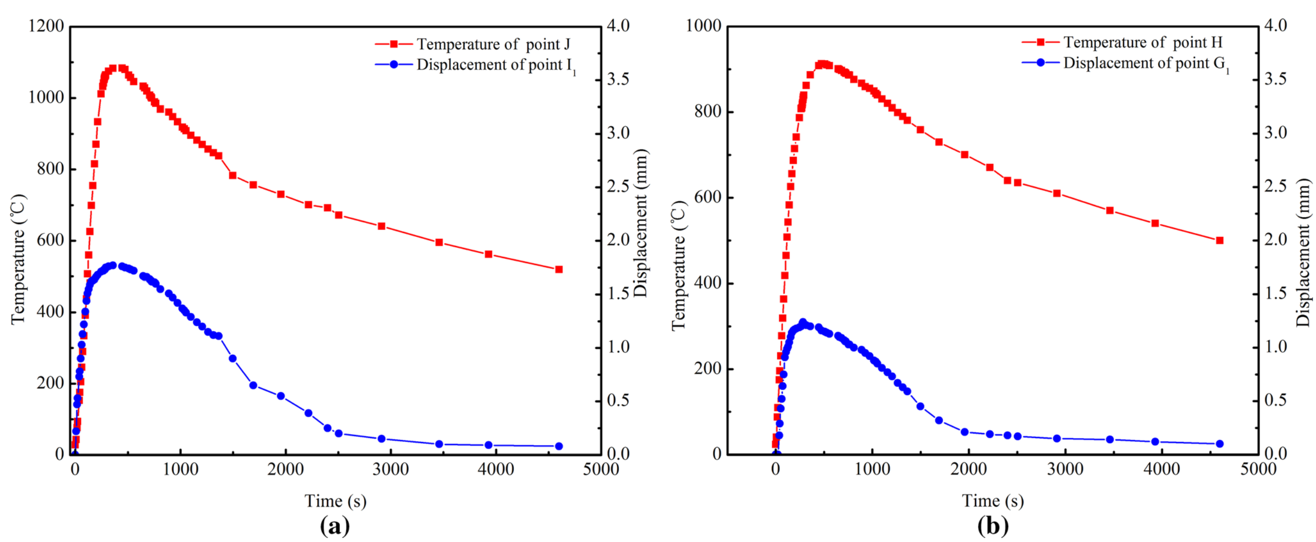

Fig. 9—Mold temperature and displacement histories measured near surface of (*a*) narrow side; (*b*) wide side.

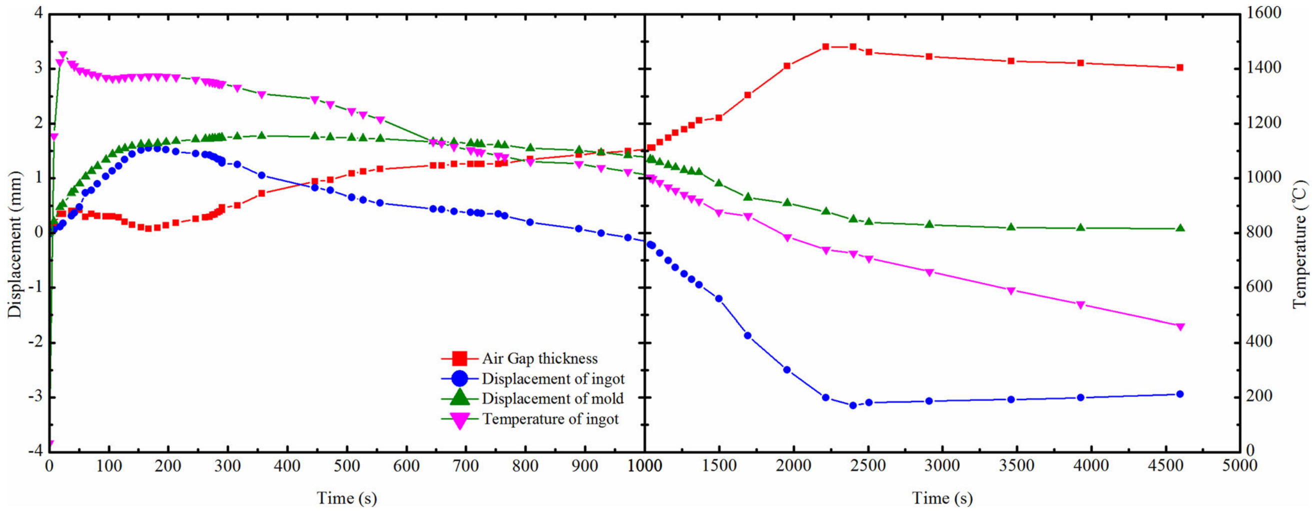

Fig. 10—Measured temperature, displacement, and air gap on the narrow side (points E and J).

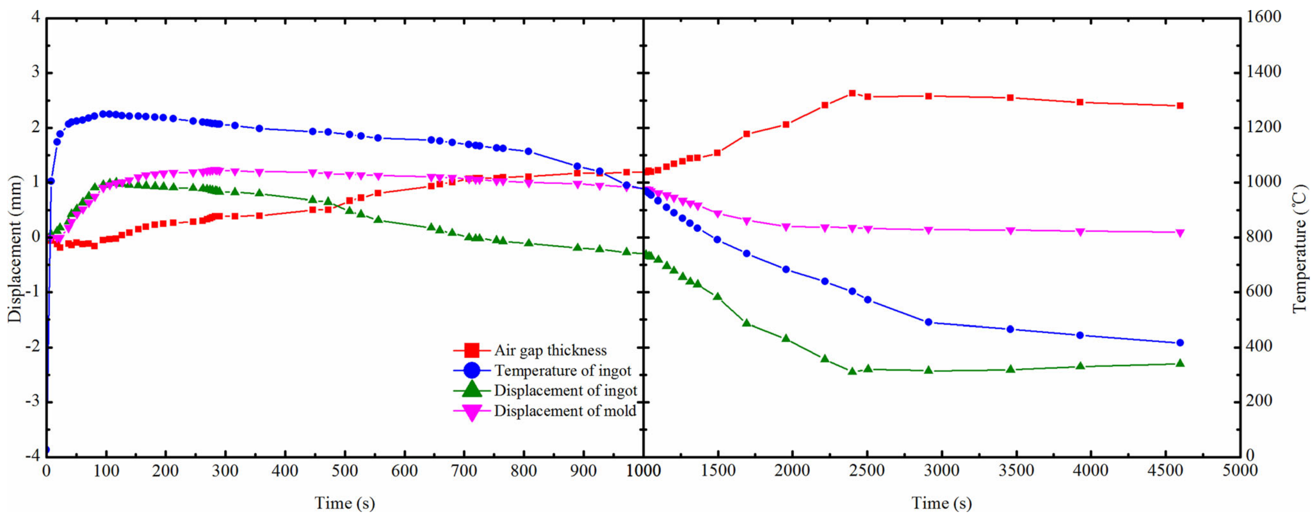

Fig. 11—Measured temperature, displacement, and air gap on the wide side (points B and H).

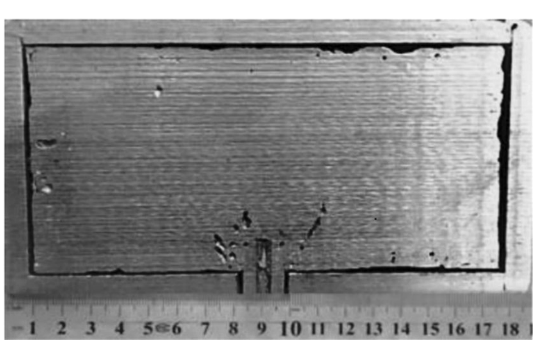

Fig. 12—Cross section through ingot and mold showing the air gap (black region) measured.

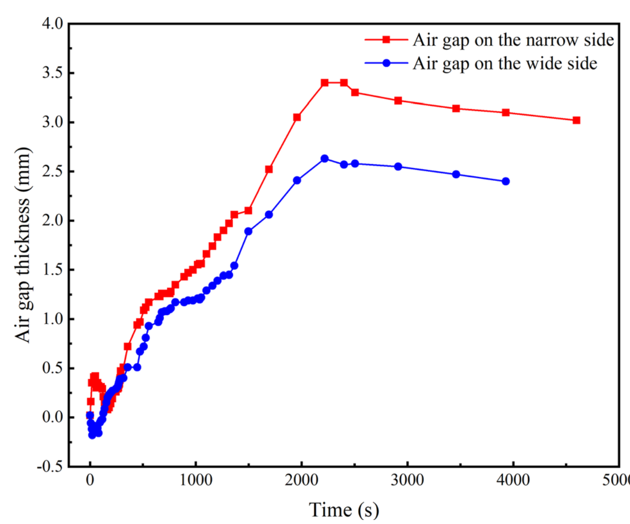

Fig. 13—Measured gap change with time on the narrow side and wide side.

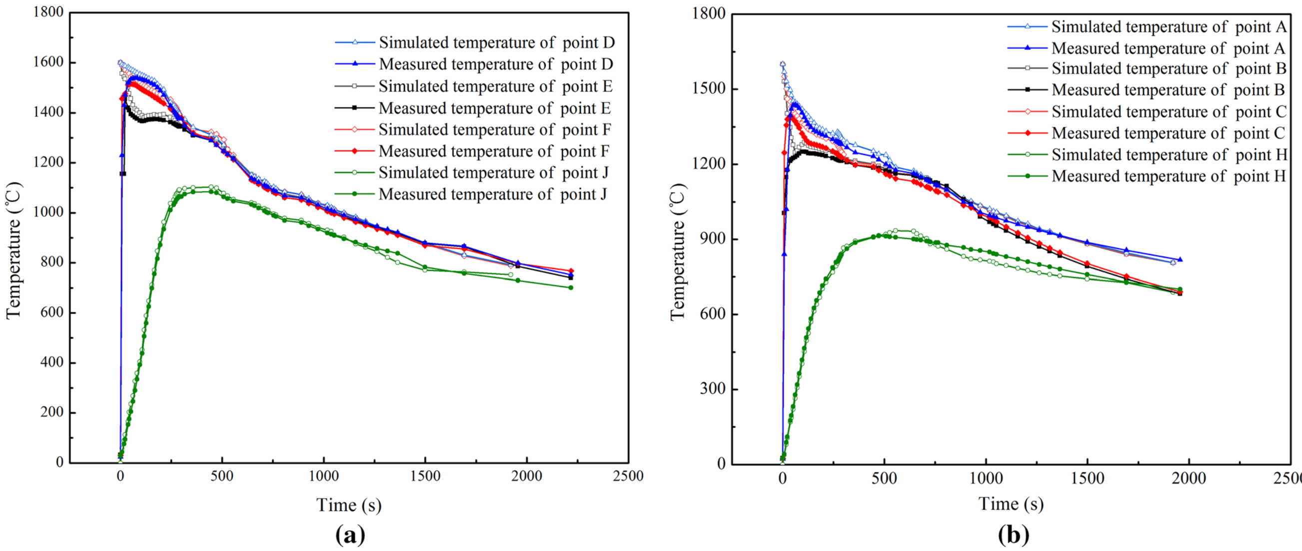

Fig. 14—Comparison of simulated and measured temperature histories in ingot and mold (*a*) narrow side; (*b*) wide side.

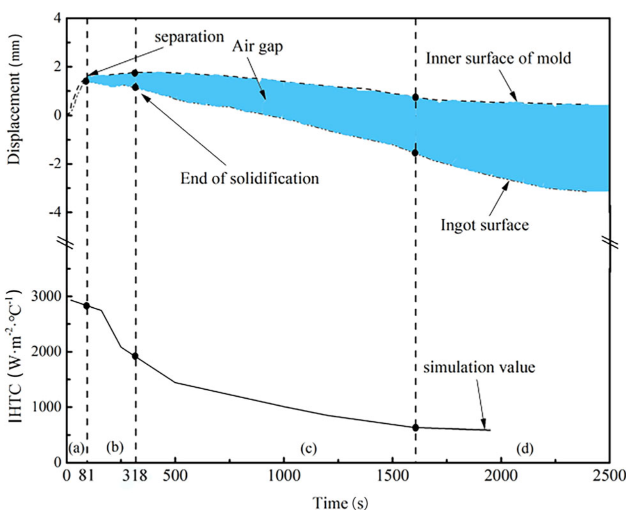

Fig. 15—Narrow side calculated interfacial heat transfer coefficient and measured gap thickness histories. (*a*) Interface contact; (*b*) interfacial air gap formation; (*c*) interfacial air gap increases; (*d*) constant interface air gap.

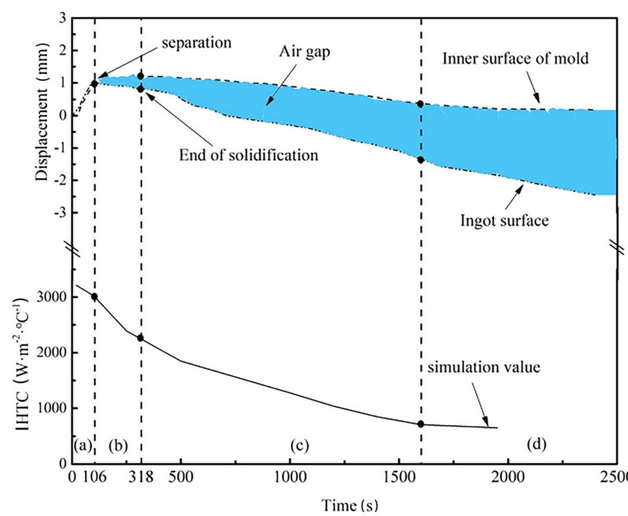

Fig. 16—Wide side calculated interfacial heat transfer coefficient and measured gap thickness histories. (*a*) Interface contact; (*b*) interfacial air gap formation; (*c*) interfacial air gap increases; (*d*) constant interface air gap.

$$q_{\text{gap}} = -k\partial T/\partial n = h(T_{\text{shell}} - T_{\text{mold}}), \quad [14]$$

$$h = h_{\text{cond}} + h_{\text{rad}}, \quad [15]$$

where q_{gap} is heat flux across the interface; n is the normal unit vector to the surface. The heat transfer coefficient due to radiation between two parallel plates[40] is given by

$$h_{\text{rad}} = \frac{\sigma}{\frac{1}{\varepsilon_{\text{shell}}} + \frac{1}{\varepsilon_{\text{mold}}} - 1}(T_{\text{shell}} + T_{\text{mold}})(T_{\text{shell}}^2 + T_{\text{mold}}^2), \quad [16]$$

where the Stefan-Boltzmann constant σ is 5.6704×10^{-8} W m^{-2} K^{-4}, $\varepsilon_{\text{shell}}$ and $\varepsilon_{\text{mold}}$ are the surface emissivities of the shell and mold surface, taken to be 0.8[40]; and T_{shell} and T_{mold} are the temperatures of shell and mold surface. Here, the shell and mold temperatures were taken at points E and J for the narrow side, as shown in Figure 7(a) and at point B and H for the wide side, as shown in Figure 7(b). These points are located 5 mm from the interface.

The heat transfer coefficient due to conduction is calculated as:

$$h_{\text{cond}} = \frac{k_{\text{air}}}{d_{\text{gap}} + d_{\text{roughness}}}, \quad [17]$$

where d_{gap} is the measured thickness of the gap, as shown in Figure 13; $d_{\text{roughness}}$ is the measured roughness of the ingot surface; and k_{air} is the average thermal conductivity of the gases in the gap. Here, the gas

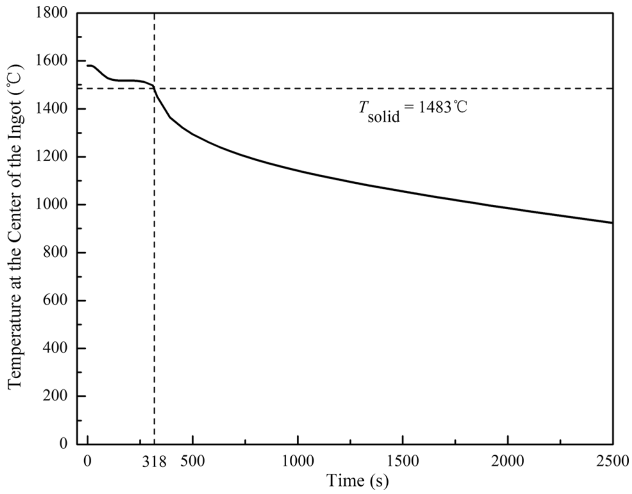

Fig. 17—Temperature evolution calculated in the ingot center.

conductivity was calibrated to be 1.1 W m^{-1} $°C^{-1}$ in order to get the best match with the measurements. This value greatly exceeds that of air, but significant amounts of hydrogen and other very conductive, volatile gases are believed to be present in the gap, owing to the presence of water vapor and oils. Water vapor sources include humidity in the air and the decomposition of oxide scale on the inner wall of the mold. A mixture of silicone oil and silicone resin was used as the release agent for the mold. Attention should be paid to these gap materials for accurate prediction of IHTC.

The IHTC calculated by the simple model, Eqs. [15] through (17), is compared with the IHTC calculated by the inverse calculation, in Figure 18(a) for the narrow side and Figure 18(b) for the wide side. The two models can be seen to be in reasonable agreement. The simple model shows significant fluctuations in IHTC during the initial stage from 10 to 200 seconds, especially on the narrow side. This is due to minor variations in the gap in the first stage of reasonably good contact between the shell and mold. The high initial IHTC during this stage is very sensitive to minor variations in contact. The maximum heat transfer coefficient found in this work, ~ 3500 W m^{-2} $°C^{-1}$, is smaller than reported previously,[19] likely due to the large surface roughness of the cast surface in this work. However, it is higher than the value of 1700 W m^{-2} $°C^{-1}$ reported in other work.[17] The IHTC then drops sharply, and then more gradually, according to the evolution of the air gap, as discussed previously.

As shown in Figure 19, during all stages, conduction is much more important than radiation across the gap, especially in the early stages when the gap is small. Later, when the gap is large, the conduction fraction drops to a constant fraction of about 70 pct of the total IHTC and is slightly higher on the wide side.

To better visualize the effect of the air gap on interfacial heat transfer coefficient, the results in Figure 18 are replotted in Figure 20 as a function of gap thickness. Here, the agreement between the inverse model and simple model, Eqs. [15] through (17), is even clearer. From an initial value that depends on surface roughness, the average IHTC decays with increasing air gap *via* the same smooth relation on both ingot sides. This is significant because the air gap and temperature histories differ between the two sides. Note that the same air gap arises at different times on a given side during the initial stage of good contact, which generates multiple points on Figure 20, but they all fall on roughly the same line. This shows that the simple model, Eqs. [15] through (17), is a reasonable way to characterize interfacial heat transfer during the casting of steel ingots, so long as the surface roughness, gap size, and gas conductivity are known.

V. CONCLUSIONS

(1) The temperature of the mold is increased after pouring and then gradually decreased after about 500 seconds. The temperature of the wide surface of the ingot is significantly lower than that of the narrow surface.
(2) The law of displacement of the ingot and mold is generally consistent with the law of temperature change. In the initial stage of pouring, the molten steel does not shrink but expands with the mold. This is because the mold expands when heated, and the molten steel will move positively with the expansion of the mold.
(3) About 160 seconds after the start of pouring, the air gap began to appear when the solidification shrinkage force was greater than the static pressure of the molten steel due to the thickening of the solidified billet shell. The amount of air gap thickness after solidification cannot reflect the amount of air gap thickness during solidification. The thickness of the air gap during the formation is linear with time.
(4) Substituting the interfacial heat transfer coefficients obtained by the inverse calculation into the forward calculation model, the obtained temperature field is in good agreement with the experimental temperature field, which indicates that the inverse calculation method and the inverse calculation results are reliable. According to the inflection point of IHTC and air gap, the influence of air gap thickness on the interface heat transfer coefficient can be divided into four stages. In the first stage, there is no air gap, and the IHTC is about ~3000 W m^{-2} $°C^{-1}$. In the second stage, air gap forms and the IHTC sharply drops. In the third stage, air gap thickness increases and the effect of air gap on IHTC is gradually weakened. In the fourth stage, the air gap thickness continues to increase but the IHTC basically remains around 600 W m^{-2} $°C^{-1}$.
(5) The interfacial heat transfer coefficient can be estimated accurately using a simple equation, Eqs. [15] through (17). The surface roughness and air gap thickness affect the IHTC together; especially the effect of the surface roughness cannot be ignored. The effect of conduction on IHTC is much more

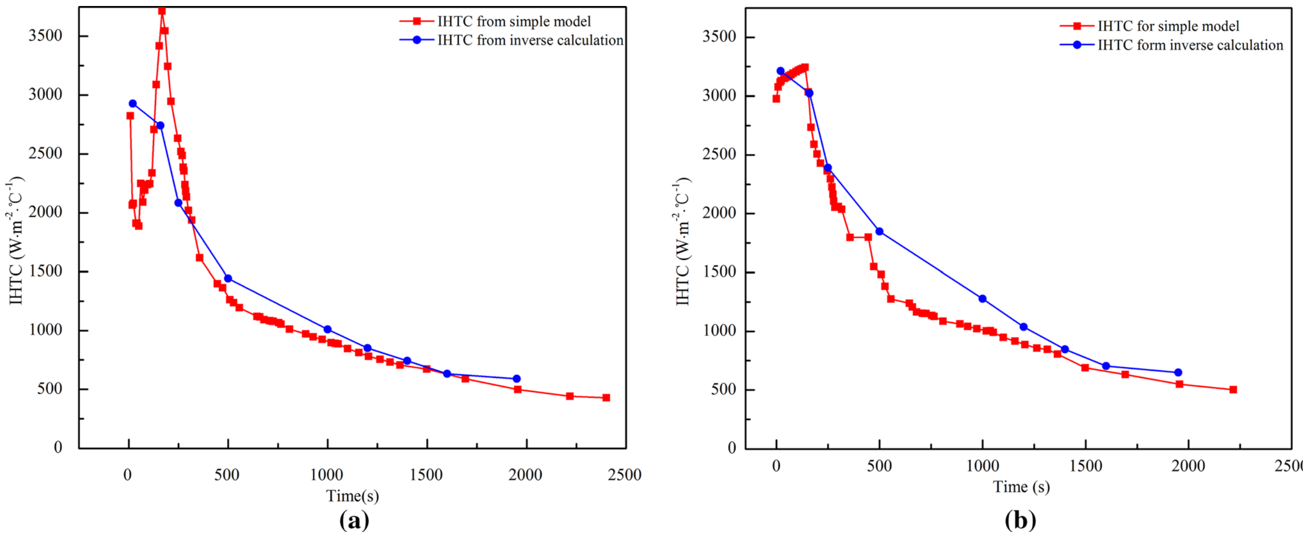

Fig. 18—Comparison of IHTC from the simple model and inverse model (*a*) narrow side; (*b*) wide side.

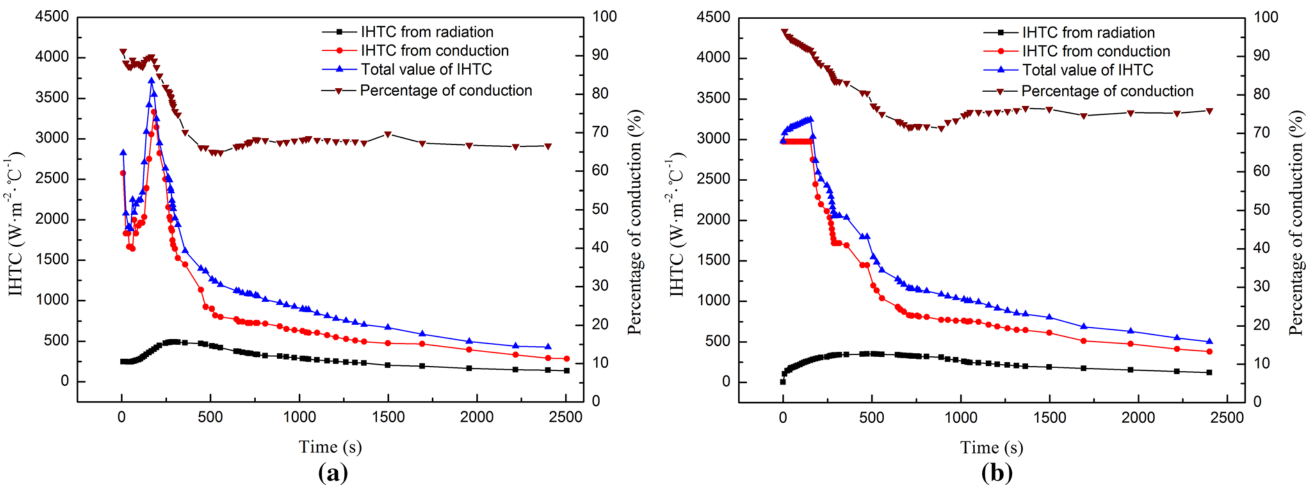

Fig. 19—IHTC calculated from radiation and conduction components (*a*) narrow side; (*b*) wide side.

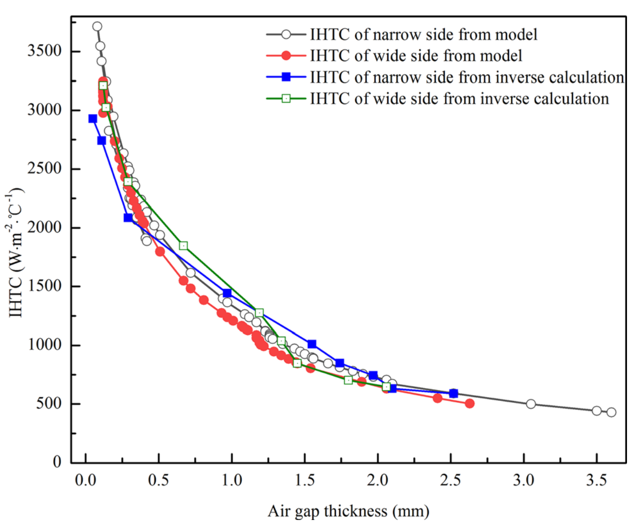

Fig. 20—The influence of air gap on interfacial heat transfer coefficient.

important than radiation across the air gap, accounting for about seventy percent of the effective IHTC, even when the gap is large, during the later stages of cooling. The gap thermal conductivity is much higher than that of air, owing to hydrogen and other conductive gases from water vapor, release agents, and other materials in the gap.

The results of this study should help to improve the accuracy of numerical simulations of the steel-ingot casting process and thereby enable quality improvements in future work.

ACKNOWLEDGMENTS

The authors gratefully express their appreciation to Natural Science Foundation of China (Nos. 51974153, U1960203, 51974156), the Joint Fund of State key

Laboratory of Marine Engineering and University of Science and Technology Liaoning (SKLMEA-USTLN-201901, SKLMEA-USTL-201707), and the China Scholarship Council (201908210457).

REFERENCES

1. L.C. Hibbeler, M.M.C. See, J. Iwasaki, K.E. Swartz, R.J. O'Malley, and B.G. Thomas: *Appl. Math. Model*, 2016, vol. 40, pp. 8530–51.
2. W.D. Griffiths: *Metall. Mater. Trans. B*, 1999, vol. 30, pp. 473–82.
3. J. Kron, T. Antonsson, and H. Fredriksson: *Int. J. Cast Met. Res.*, 2002, vol. 14, pp. 275–85.
4. R.J. Sarjant and M.R. Slack: *J. Iron Steel Inst.*, 1954, vol. 177, pp. 428–44.
5. B. Gerin, H. Combeau, M. Založnik, I Poitrault, and M Cherif: Prediction of solidification structures in a 9.8 tonne steel ingot. MCWASP XV 2020, IOP Conference Series: Materials Science and Engineering, Volume 861, MCWASP XV: International Conference on Modelling of Casting, Welding and Advanced Solidification Processes 22-23 June 2020, Jönköping, Sweden.
6. Y. Nishida, W. Droste, and S. Engler: *Metall. Mater. Trans. B*, 1986, vol. 17, pp. 833–44.
7. Z.G. Xu, X. Wang, and M. Jiang: *Steel Res. Int.*, 2017, vol. 88, pp. 231–42.
8. S.K. Choudhary, S. Ganguly, A. Sengupta, and V. Sharma: *J. Mater. Process. Technol.*, 2017, vol. 243, pp. 312–21.
9. Y.M. Dakhoul, R. Farmer, S.L. Lehoczky, and F.R. Szofran: *J. Cryst. Growth*, 1988, vol. 86, pp. 49–55.
10. W.M. Li, X.M. Zang, H.Y. Qi, D.J. Li, and X. Deng: *High Temp. Mater. Proc.*, 2019, vol. 38, pp. 672–82.
11. L.G. Zhu and R.V. Kumar: *Ironmaking & steelmaking*, 2007, vol. 34, pp. 76–82.
12. K.N. Prabhu and W.D. Griffiths: *Int. J. Cast Met. Res.*, 2001, vol. 14, pp. 147–55.
13. V.E. Bazhenov, A.V. Koltygin, Yu.V. Tselovalnik, and A.V. Sannikov: *Russ. J. Non-ferr met.*, 2017, vol. 58, pp. 114–23.
14. D. Robinson and R. Palaninathan: *Finite Elem. Anal. Des.*, 2001, vol. 37, pp. 85–95.
15. I. Stone, M. Ward, and R.C. Reed: *Mater. Sci. Forum*, 2013, vol. 765, pp. 276–80.
16. J. Kron, M. Bellet, A. Ludwig, B. Pustal, J. Wendt, and H. Fredriksson: *Int. J. Cast Met. Res.*, 2004, vol. 17, pp. 295–310.
17. B.G. Thomas, I.V. Samarasekera, and J.K. Brimacombe: *Metall. Trans. B*, 1987, vol. 18B, pp. 119–30.
18. F. Oeters, K. Ruttiger and H.J. Selenz: Casting and Solidification of Steel, 1977, vol. 1, pp. 125-67.
19. 19. R.E. Smelser and O. Richmond: Mod. Cast. Weld. Proc. IV, Palm Coast, FL, 1988, pp. 313-28.
20. J. Kron, A. Lagerstedt, and H. Fredriksson: *Int. J. Cast Met. Res.*, 2005, vol. 18, pp. 29–40.
21. C. Li and Brian G. Thomas: *Metall. Mater. Trans. B*, 2004, vol. 35B, pp. 1151-72.
22. F. Yigit and L.G. Hector: *J. Appl. Mech.*, 2000, vol. 67, pp. 66–76.
23. N. Zabaras, Y. Ruan, and O. Richmond: *J. Appl. Mech.*, 1991, vol. 58, pp. 865–71.
24. S. Engler, D. Boenisch, and B. Kohler: *AFS Cast Metals Res. J.*, 1973, vol. 9, pp. 20–30.
25. J. Savage: *J. Iron Steel Inst.*, 1962, vol. 11, pp. 260–77.
26. R.H. Tien and V. Koump: *J. Appl. Mech.*, 1969, vol. 36, pp. 763–67.
27. O. Richmond and R.H. Tien: *J. Mech. Phys. Solids*, 1971, vol. 19, pp. 273–84.
28. C.M. Raible, H. Fredriksson and S. Oestlund: *Modelling of heat flow and solidification process in a strip caster*, 2nd ed, Minerals, Metals and Materials Society, Warrendale PA, United States, 1995, pp. 817-24.
29. J. Mahmoudi and H. Fredriksson: *J. Mater. Sci.*, 2000, vol. 35, pp. 4977–87.
30. S. Berg, J. Dahlström, and H. Fredriksson: *ISIJ Int.*, 1995, vol. 35, pp. 876–85.
31. A. Lagerstedt, J. Kron, F. Yosef, and H. Fredriksson: *Mat. Sci. Eng. A*, 2005, vol. 413, pp. 44–51.
32. Y. Dong, K. Bu, Y. Dou, and D. Zhang: *J. Mater. Process. Technol.*, 2011, vol. 211, pp. 2123–31.
33. C.A. Santos, J. Quaresma, and A. Garcia: *J. Alloys Compd.*, 2001, vol. 319, pp. 174–86.
34. K. Narayan Prabhu, H. Mounesh, K.M. Suresh and A. A. Ashish: *Int. J. Cast Met. Res.*, 2003, vol.15, pp. 565–71.
35. G. Milano and F. Scarpa: Universita di Genova, Italia, private communication, 1994.
36. M. Rappaz, J.-L. Desbiolles, J.-M. Drezet, C.-A. Gandin, A. Jacot, and P. Thévoz: in Modeling of Casting, Welding and Advanced Solidification Processes, M. Cross and J. Campbell, eds., TMS, Warrendale, PA, 1995, pp. 449-57.
37. J.M. Drezet, M. Rappaz, G.U. Grün, and M. Gremaud: *Metall. Mater. Trans. A*, 2000, vol. 31, pp. 1627–34.
38. B.G. Thomas, I.V. Samarasekera, and J.K. Brimacombe: *Metall. Mater. Trans. B*, 1987, vol. 18, pp. 119–30.
39. P. Sun, W. Li, and Q.L. Ji: *China Water Transp.*, 2010, vol. 10, pp. 235–36.
40. M.L. Zappulla, S.M. Cho, S. Koric, H.J. Lee, S.H. Kim, and B.G. Thomas: *J. Mater. Process. Technol.*, 2020, vol. 278, pp. 1–14.